





Supporting Information

Nonquantal Transmission at the Vestibular Hair Cell-Calyx Synapse: K_{LV} Currents Modulate Fast Electrical and Slow K⁺ Potentials

Aravind Chenrayan Govindaraju^{a,b} , Imran H. Quraishi^c , Anna Lysakowski^d ,
Ruth Anne Eatock^e , Robert M. Raphael^{b,1} 

^a Applied Physics Graduate Program, Smalley-Curl Institute, Rice University, Houston, TX 77005;

^b Department of Bioengineering, Rice University, Houston, TX 77005;

^c Department of Neurology, Yale University School of Medicine, New Haven, CT 06510;

^d Department of Anatomy and Cell Biology, University of Illinois at Chicago, IL 60612;

^e Department of Neurobiology, University of Chicago, Chicago, IL 60637;

¹ To whom correspondence may be addressed. Email: raphael@rice.edu

This PDF file includes:

[Computational Methods:](#)

[General Modelling of Membrane Currents](#), [Governing Equations](#), [Model Simulation and Solver Conditions](#)

Figures [S1](#), [S2](#), [S3](#), [S4](#), [S5](#)

Tables [S1](#), [S2](#), [S3](#), [S4](#), [S5](#), [S6](#), [S7](#), [S8](#)

[Channel Distribution and Kinetics](#)

[Model Repository](#)

[Notes: cleft width](#), [ions needed to change \$E_K\$ vs \$V_m\$](#) , [effects of external \$\[K^+\]\$ on \$g_{K,L}\$](#) , [effects of series resistance](#)

[Experimental Methods](#)

[SI References](#)

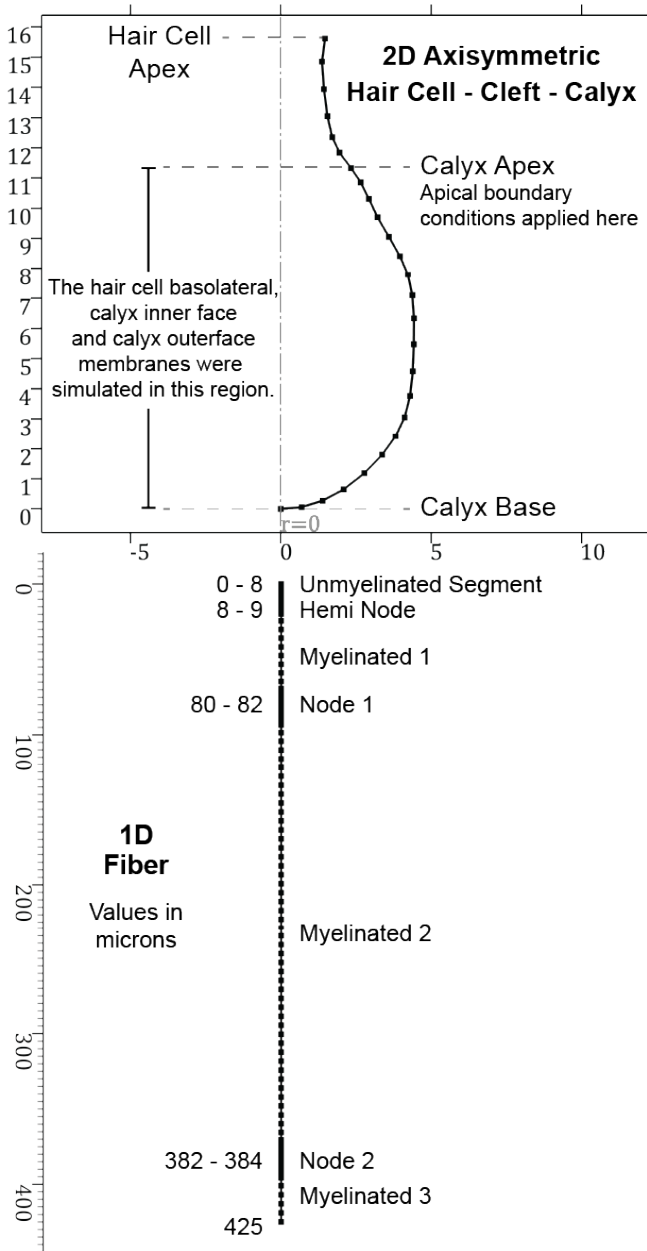
Computational Methods

Overview. The Vestibular Hair Cell-Calyx (VHCC) model incorporates information on synapse morphology, ion transporters and ion channels expressed in type I hair cells (channel types: mechanotransduction (MET), K_v , Ca_v , HCN; transporter: Na^+/K^+ -ATPase), and in calyces and afferent fibers (channel types: K_v , Na_v , HCN; transporters: KCC, Na^+/K^+ -ATPase) (see **Fig. 1** in main text). The dynamic behavior of the system is determined from measured or estimated channel open probabilities, time constants and whole-cell conductances, and from assumptions (which we describe) about the activity of ion transporters based on literature. We implemented the VHCC model with finite element analysis simulation software, using equations for K^+ and Na^+ electro-diffusion in the cleft, Hodgkin-Huxley-style equations to represent voltage-dependent ion flow through ion channels, and the cable equation for electrical propagation. For each simulation, steady-state conditions are established and followed by a step or sinusoidal deflection of the hair bundle or voltage step; outputs include the basal-to-apical gradients within the synaptic cleft for K^+ , Na^+ and electrical potential, and voltage across the hair-cell-facing postsynaptic membrane of the calyx (“calyx inner face”), and in the hemi-node and first two full nodes of the distal branch of the bipolar vestibular afferent neuron. The distal branch connects the synaptic terminals on hair cells (in this case a single calyx) to the neuronal cell body in the vestibular ganglion; the remainder of the distal branch, the cell body and the central branch projecting to the brain are not included in the model. Negative currents represent the flow of cations into the compartment bearing the channel or transporter in its membrane. The hair cell is assumed to be equipotential based on its small overall size, compact form and low intracellular resistance. Intracellular ion concentrations ($[K^+] = 150$ mM; $[Na^+] = 12$ mM) within the hair cell and calyx are the same and are assumed constant over the course of the simulation as these spaces are much greater in volume than the synaptic cleft. Details of model development are described below.

Model Geometry. The model was designed with the COMSOL Multiphysics 5.6 software package. We used a 2D axisymmetric finite element boundary to represent the hair cell, synaptic cleft, and afferent calyx and a 1D finite element line to represent the afferent fiber ([Fig. S1](#)). The 2D boundary used to represent the hair cell (H), synaptic cleft (SC), the calyx inner face (CIF) and calyx outer face (COF) is an interpolation curve generated from (R,Z) coordinates of the perimeter of a central-zone type I hair cell and calyx from the central zone of the sensory epithelium of a crista in an adult Long-Evans rat (shown in Fig. 2C of Lysakowski et al. 2011; similar calyces from the striolar zone of the rat utricle are shown in our

Fig. 1A). The dimensions and interpolated points used to create the representative geometry in Comsol 5.6 are shown in [Fig. S1](#). HN, N and M indicate the hemi-node, nodes and myelinated sections (inter-nodes) of the afferent fiber, respectively. In both 2D (hair cell and calyx) and 1D (fiber) geometries, local properties such as the conductance density for each channel type, steady state expressions for channel gating variables and gating time constants were defined. Note that the apex of the calyx occurred at 11.3 μm relative to the calyx base for all simulations in the manuscript, except for the variations in calyx height presented in **Fig. 7**.

Finite Element Mesh in Comsol



Geometric Parameters

Hair-Cell-Calyx Geometry Interpolation Points	
R (μm)	Z (μm)
1.47	15.61 (Hair-Cell Apex)
1.39	14.33
1.5	13.44
1.61	12.72
1.89	11.94
2.33	11.33 (Calyx Apex)
3.16	9.8
4.03	8.28
4.42	5.24
4.03	2.83
2.56	1
1.72	0.43
0	0 (Calyx Base)

Calculated Areas	Values
a_H	$340.21 \mu\text{m}^2$
$a_{H,C}$	$294.63 \mu\text{m}^2$
a_{CIF}	$294.63 \mu\text{m}^2$
a_{COF}	$288.33 \mu\text{m}^2$
$a_{F,HN}$	$3\pi \mu\text{m}^2$
$a_{F,N}$	$6\pi \mu\text{m}^2$
$a_{F,Unmyel}$	$24\pi \mu\text{m}^2$

Cleft width (d_{SC})	$0.02 \mu\text{m}$
Calyx width (d_C)	$1 \mu\text{m}$
Fiber Radius (r_F)	$1.5 \mu\text{m}$

Fig. S1 – Hair Cell-Calyx and Fiber Geometries in the COMSOL 5.6 GUI.

The 2D axisymmetric mesh representing the hair cell, synaptic cleft and calyx (top) was modelled based on the geometry of a type I hair-cell-calyx synapse from central/striolar zones of rodent vestibular organs. Dots in the above geometry represent finite element nodes, and lines represent connecting edge elements. The interpolation points were based upon the geometry of a hair cell and calyx reported in Fig. 2C of Lysakowski et al. (2011). The calyx width d_C was obtained from the same calyx. The width of the synaptic cleft d_{SC} was obtained from Spoendlin (1966). The fiber radius (r_f) is based on experimental measurements (Lysakowski et al. 1995; Hoffman and Honrubia 2002). The fiber end was treated as a closed boundary. Location of the hemi-node and the first node were estimated from confocal micrographs (Lysakowski et al. 2011). $a_{H,C}$ denotes the surface area of the hair cell within the calyx.

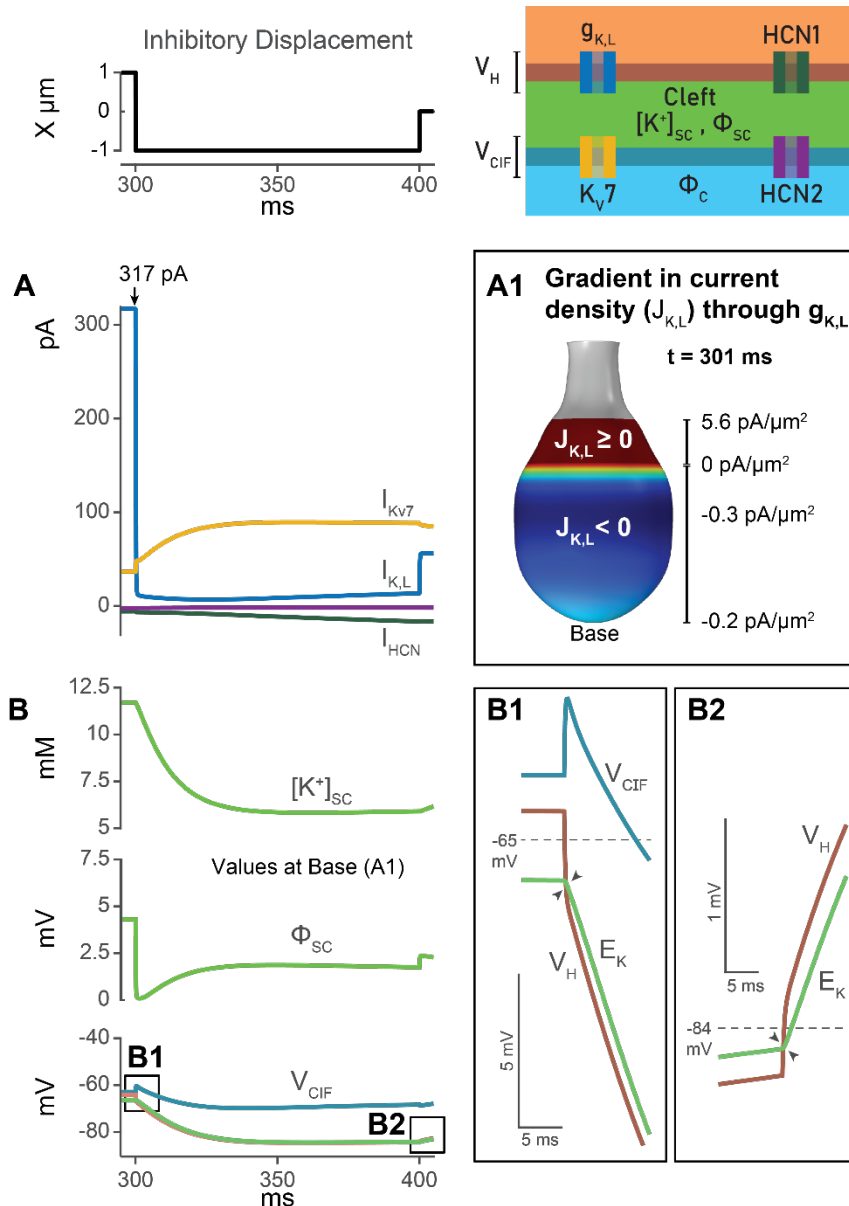


Fig. S2 – Gradients in current density exist from base to apex of the synaptic cleft.

(A) Net currents through $g_{K,L}$ (hair cell, blue), K_v7 (calyx, gold) and HCN channels (hair cell, dark green, and calyx, purple) following the onset of the full negative step. (A1) Gradient in current density through $g_{K,L}$ 1 ms after the negative step at 300 ms. Small currents flow into the hair cell in basal regions, and larger currents flow out of the hair cell near the apical regions of the synaptic cleft. The direction and magnitude of the current results from the difference between V_H and E_K which varies from base to apex and with the ongoing stimulus. This behavior is illustrated at the base of the synapse in B, B1 and B2.

(B) $[K^+]_{SC}$, Φ_{SC} , V_H , V_{CIF} and E_K at the base of the synapse during inhibitory stimuli. Note the crossover of V_H and E_K following the onset (B1) and the termination (B2) of the negative step. As the driving force for currents is $(V_H - E_K)$, the separation between the V_H and E_K curves determines current magnitude and current direction is outward if V_H is positive to E_K . During the negative steps, currents through $g_{K,L}$ in the basal regions in A1 are inward because V_H is negative to E_K .

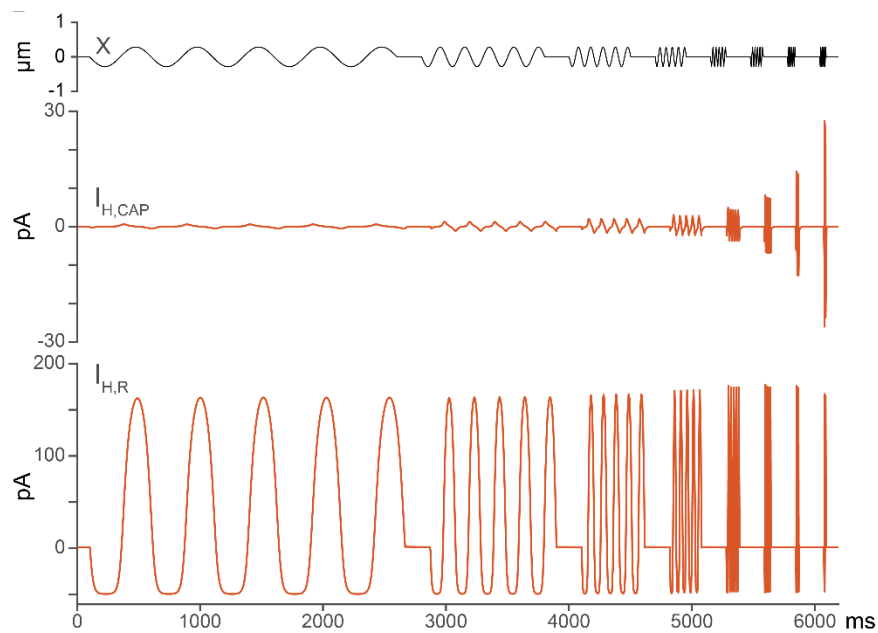


Fig. S3 – Resistive currents dominate capacitive currents during sinusoidal bundle stimulation
 Capacitive ($I_{H,CAP}$) and resistive ($I_{H,R}$) currents from the hair cell during bundle stimulation modeled in Figure 5 in the manuscript. $I_{H,R}$ is the primary contributor to changes in the synaptic cleft during sinusoidal bundle displacement. Note the different scale of the Y-axis for the capacitive and resistive currents. A small stimulus ($\pm 0.3 \mu\text{m}$) was used to avoid triggering APs and better reveal the underlying changes in hair cell currents.

The VHCC model enables us to track the contributions of capacitive and resistive currents to NQT as a function of frequency ([SI Eqs. S3-5, S8-13](#)). The model predicts that resistive currents ($I_{H,R}$) are much larger than capacitive current ($I_{H,CAP}$) flowing from the type I hair cell. The capacitive current does increase with frequency, as expected, and can noticeably affect NQT during large voltage step stimuli (discussed in [Fig. 6](#)).

Table S1 - Abbreviations

H, C, SC, CIF, COF, F	Subscripts denote the hair cell (H), calyx (C), synaptic cleft (SC), calyx inner face (CIF), calyx outer face (COF) and fiber (F) respectively.
$\phi_H, \phi_C, \phi_{SC}, \phi_F$	Electrical potential in the hair cell, calyx, synaptic cleft, and fiber respectively.
ρ_F	Resistivity of the afferent fiber.
$[K^+]_{SC}, [Na^+]_{SC}$	K^+, Na^+ concentrations in the synaptic cleft
c_H	Total hair cell capacitance
C_m	Specific membrane capacitance
Ca_V, K_V, Na_V	Voltage-gated calcium, potassium, and sodium channels
D_K, D_{Na}	Effective diffusion coefficients for K^+, Na^+ in the synaptic cleft
d_{SC}	Width of the synaptic cleft
$g_{x,max}$	Maximum whole-cell conductance of specific channel type
$G_{x,max}$	Maximum conductance density of specific channel type
$g_{K,L}$	Low-voltage-activated potassium conductance of type I hair cells
HCN	Hyperpolarization-activated cyclic nucleotide-gated (channels)
I_{MET}	Mechanotransduction current
J_x	Current density through channel or transporter 'x'
J_{M_x}	Current density through membrane 'x'
KCC	Potassium Chloride Cotransporter
K_V7	Voltage-gated potassium channels formed by subunits encoded by the KCNQ gene family
P_{open}	Channel open probability
$VHCC$	Vestibular Hair Cell-Calyx
V_m	Membrane voltage

Table S2 – Equilibrium Potentials and Voltages Across Membranes

Property			Hair Cell (H)	Calyx inner face (CIF)	Calyx outer face (COF)	Fiber (F) HN N M
E_K	K ⁺ Equilibrium Potential	mV	$26 \cdot \ln \left(\frac{[K^+]_{sc}}{150} \right)$	$26 \cdot \ln \left(\frac{[K^+]_{sc}}{150} \right)$	$26 \cdot \ln \left(\frac{[K^+]_{sc}}{150} \right) = -88.4$	-88.4
E_{Na}	Na ⁺ Equilibrium Potential	mV	$26 \cdot \ln \left(\frac{[Na^+]_{sc}}{12} \right)$	$26 \cdot \ln \left(\frac{[Na^+]_{sc}}{12} \right)$	$26 \cdot \ln \left(\frac{140}{12} \right) = 63.8$	63.8
V_m	Membrane Voltage	mV	$\phi_H - \phi_{sc}$	$\phi_C - \phi_{sc}$	ϕ_C	ϕ_F

General Modeling of Membrane Currents

Membrane channels and transporters were distributed in the various compartments based on experimental observations ([Table S6](#), [S7](#)). Abbreviations used for ion channels and other parameters are listed in [Table S1](#). For each type of ion, local current density through a particular channel type 'x' was described by [Eq. S1](#):

$$J_{ion,x} = G_{x,max} \cdot P_{x,open} \cdot (V_m - E_{ion}) \quad (S1)$$

$G_{x,max}$ is the maximum conductance density through a channel 'x' per unit area of membrane, obtained by dividing the maximum whole-cell conductance, $g_{x,max}$, by the surface area of the relevant membrane. $P_{x,open}$, calculated as a function of channel gating variables using the Hodgkin-Huxley formalism, is the percentage of the maximal conductance available. The equations describing the kinetics of channel gating variables as functions of membrane voltage and current densities through each channel type are available in [Table S6](#). V_m is the transmembrane potential as defined in [Table S2](#) for each membrane in the model. E_{ion} is the equilibrium potential of the ion species across the membrane and is continuously updated as the ion concentration changes in the synaptic cleft. In the notation for current densities, K, Na, O, indicate the potassium, sodium, and other ions such as Ca^{2+} or Cl^- . Current densities and fluxes, J , through channels and transporters were summed to describe the current densities of ionic species across Hair cell (H) and Calyx Inner Face (CIF) or Calyx Outer Face (COF) membranes. The species currents were in turn summed to obtain the total current densities through each membrane (J_{MH} , J_{MCIF} , J_{MCOF} , J_{MF}) ([Table S3](#)).

Table S3– Local and Net Current Densities Across Individual Membranes

J_{KH}	$J_{K,L} + J_{K,HCN1} + J_{K,NaK}$	J_{NaCIF}	$J_{Na,HCN2} + J_{Na,NaK}$	J_{MH}	$J_{KH} + J_{NaH} + J_{OH}$
J_{NaH}	$J_{Na,HCN1} + J_{Na,NaK}$	J_{OCIF}	$-J_{KCC4}$	J_{MCIF}	$J_{KCIF} + J_{NaCIF} + J_{OCIF}$
J_{OH}	J_{Ca}	J_{KCOF}	$J_{K,HCN2} + J_{K,NaK}$	J_{MCOF}	$J_{KCOF} + J_{NaCOF} + J_{Leak}$
J_{KCIF}	$J_{KV7.4} + J_{KV11.1} + J_{K,HCN2} + J_{K,NaK} + J_{KCC4}$	J_{NaCOF}	$J_{Na,HCN2} + J_{Na,NaK}$	J_{MF}	$J_{KV7.x} + J_{KV1.x} + J_{KV3.4} + J_{NaV1.x}$

See [Table S6](#) for equations of current densities and kinetics for each channel type.

Governing Equations

Continuity equations describe the electric potential and ion concentrations in the various compartments (Quraishi 2008).

Hair Cell Electrical Potential (ϕ_H). The time dependence of the hair cell electrical potential is calculated as a function of hair cell capacitance (c_H), mechanotransduction current (I_{MET}), and current across the basolateral membrane:

$$c_H \frac{\partial \phi_H}{\partial t} = -I_{MET} - \int_0^L 2\pi r \left(J_{MH} - C_m \frac{\partial \phi_{SC}}{\partial t} \right) ds \quad (S2)$$

I_{MET} is calculated according to a peak current-displacement relationship (Holt et al. 1997) and a maximal conductance of 5 nS, based on ~50 transduction channels of ~100-pS single-channel conductance (Corey et al. 2019). We calculated the total capacitance of the hair cell ($c_H = 6.4$ pF) by multiplying the surface area of the cell by the specific capacitance of the membrane (C_m). L is the length of the synaptic cleft from base to apex; ds is an infinitesimal increment of the arclength of the cleft. The integral represents the total current across the hair cell basolateral surface within the calyx.

Concentration and Electro-diffusion in the Synaptic Cleft. $[K^+]_{SC}$ and $[Na^+]_{SC}$ were calculated with the Nernst-Planck electro-diffusion equation for each ion:

$$\frac{\partial [K^+]_{SC}}{\partial t} = \nabla \cdot (D_K \nabla [K^+]_{SC}) + \nabla \cdot \left(D_K \frac{F}{RT} [K^+]_{SC} \nabla \phi_{SC} \right) + \frac{1}{d_{SC}} \frac{(J_{KH} + J_{KClF})}{F} \quad (S3)$$

$$\frac{\partial [Na^+]_{SC}}{\partial t} = \nabla \cdot (D_{Na} \nabla [Na^+]_{SC}) + \nabla \cdot \left(D_{Na} \frac{F}{RT} [Na^+]_{SC} \nabla \phi_{SC} \right) + \frac{1}{d_{SC}} \frac{(J_{NaH} + J_{NaClF})}{F} \quad (S4)$$

D_K , the effective diffusion coefficient for K^+ , is calculated by dividing the diffusion coefficient of K^+ in aqueous solution at 25 °C: $1.957 \cdot 10^{-9} \frac{m^2}{s}$ (Lide 2005) by the square of the tortuosity coefficient 1.55 (Nicholson and Phillips 1981), yielding $D_K = 0.81 \cdot 10^{-9} \frac{m^2}{s}$. Similarly, $D_{Na} = 0.56 \cdot 10^{-9} \frac{m^2}{s}$. The volume of the synaptic cleft is assumed to be constant and the width (d_{SC}) and length of the synaptic cleft are fixed.

Electrical Potential in the Synaptic Cleft (ϕ_{SC}). At bouton synapses, the electrical potential in the synaptic cleft, ϕ_{SC} , is assumed to be that of the extracellular medium (at reference potential or ground, ~0 mV) because the resistance of the cleft is assumed to be low. At the VHCC synapse, in contrast, the

extended synaptic cleft created by the calyx geometry poses an increased resistance and large K^+ currents that flow during transduction may allow a significant cleft potential. ϕ_{SC} was calculated following the law of charge conservation as a function of the resistive and capacitive currents across both pre-synaptic (hair cell) and post-synaptic (calyx) membranes, as well as electro-diffusion of ions:

$$(2C_m) \frac{d\phi_{SC}}{dt} = C_m \frac{d\phi_H}{dt} + C_m \frac{d\phi_{calyx}}{dt} + J_H + J_{CIF} + \nabla \cdot (FD_K \nabla [K^+]_{SC}) \cdot d_{SC} + \nabla \cdot (FD_{Na} \nabla [Na^+]_{SC}) \cdot d_{SC} + \nabla \cdot \left(\left(\sigma_{O_{SC}} + \frac{D_K [K^+]_{SC} F^2}{RT} + \frac{D_{Na} [Na^+]_{SC} F^2}{RT} \right) \nabla \phi_{SC} \right) \cdot d_{SC} \quad (S5)$$

At room temperature, the terms $\frac{D_K [K^+]_{SC} F^2}{RT} + \frac{D_{Na} [Na^+]_{SC} F^2}{RT}$ resolve to $\sim 300 - 400$ nS/ μ m when $[K^+]_{SC}$ and $[Na^+]_{SC}$ range between 5-40 and 120-140 mM, respectively. The total conductivity contribution from ions ($\sigma_{O_{SC}}$) other than K^+ and Na^+ is set equal to 600 nS/ μ m to be consistent with the 1000 nS/ μ m used in the calyx and afferent fiber. 1000 nS/ μ m (equivalent to 1 S/m) is within the conductivity range (0.75 – 1.45 S/m) reported from measurements in tumor cells (Wang et al. 2017), hippocampal neurons (Zhou et al. 2016) and cerebrospinal fluid (Baumann et al. 1997). The diffusion of other ions, e.g., chloride, was not explicitly considered and their concentrations within the synaptic cleft are assumed to be constant and a part of the $\sigma_{O_{SC}}$ term.

Electrical Potential in the Calyx (ϕ_C). The electrical potential within the calyx was calculated as a function of the resistive and capacitive currents across both the post-synaptic membrane and the calyx outer face membranes as well as the longitudinal current from the afferent fiber.

$$(2C_m) \frac{d\phi_C}{dt} = C_m \frac{d\phi_{SC}}{dt} + \nabla \cdot (\sigma_C d_C \nabla \phi_C) - J_{CIF} - J_{COF} - J_F \quad (S6)$$

The current from the fiber to the calyx, J_F , is equal to $(-\pi \cdot \frac{r_f}{\rho_l} \cdot u_x)$, where r_f the radius of the fiber is 1.5 μ m, ρ_l the longitudinal resistivity is 1 M Ω μ m, and u_x is the longitudinal potential gradient within the fiber. The fiber radius used is comparable to diameters reported for calyx afferents (Hoffman and Honrubia 2002).

Electrical Potential in the Afferent Fiber (ϕ_F). To describe the potential in the afferent fiber, ϕ_F , we implemented the cable equation along the 1D line representing the fiber:

$$r_F^2 \frac{d^2 \phi_F}{dx^2} = 2r_F \rho_l C_m \frac{d\phi_F}{dt} - 2r_F \rho_F J_{MF} \quad (S7)$$

Channel gating variables and conductance densities (see [Table S6](#)) were defined for the hemi-node, nodes and myelinated regions of the fiber as shown in **Fig. 1**. Gating variables for channels present on the fiber were treated similarly to those on the calyx and hair cell.

Initial and Boundary Conditions. Before running the simulation, the initial value of ϕ_H was set at -75 mV, within the normal range of reported resting potentials for rodent type I hair cells (Rennie and Correia 1994; Rennie et al. 1996; Rüschi and Eatock 1996; Chen and Eatock 2000; Lim et al. 2011; Spaiardi et al. 2017). Where necessary, initial values of ϕ_H were varied ± 10 mV to assist solver convergence. An initial value of 0 mV was used for the potential in the synaptic cleft, ϕ_{SC} . The boundary condition $\phi_{SC} = 0$ mV was applied at the apical end of the synaptic cleft. An initial value of -70 mV was used for ϕ_{Calyx} and ϕ_F , consistent with recorded resting potentials in rodent calyces ranging from -60 to -70 mV in (Meredith and Rennie 2015; Sadeghi et al. 2014; Songer and Eatock 2013). The boundary condition $\phi_{Calyx} = \phi_F$ was applied at the base of the calyx and the far end of the fiber was treated as a closed boundary. $[K^+]_{SC}$ and $[Na^+]_{SC}$ were given initial values of 5 mM and 140 mM, respectively, throughout the cleft, based on the external (bath) recording solutions of electrophysiological data referenced in the model and similar to perilymph facing the outer face of the calyx and other extracellular fluids. K^+ and Na^+ concentrations were pinned at these values at the apical end of the cleft but were allowed to vary elsewhere within the cleft. To better understand non-quantal transmission (NQT), we altered the initial conditions to independently analyze the contributions of changes in the synaptic cleft in (1) electrical potential and (2) potassium concentration. As described below, this theoretical exercise gave greater insight into the mechanisms of NQT.

Table S4 – Initial and Boundary Conditions

Parameter	Value	Reference
$\phi_{H,init}$	-75 mV	Correia and Lang 1990; Rennie and Correia 1994; Rennie et al. 1996; Rüsç and Eatock 1996; Chen and Eatock 2000; Lim et al. 2011; Spaiardi et al. 2017
$\phi_{SC,init}$	0 mV	Based on the external (bath) recording solutions of electrophysiological data referenced in the model
$\phi_{SC,apical}$	0 mV	
$[K^+]_{SC,init}$ $[K^+]_{SC,apical}$	5 mM	
$[Na^+]_{SC,init}$ $[Na^+]_{SC,apical}$	140 mM	
$\phi_{C,init}$	-70 mV	Meredith and Rennie 2015; Sadeghi et al. 2014; Songer and Eatock 2013
$\phi_{F,init}$	-70 mV	Assumed continuous with $\phi_{C,init}$

ϕ_{SC} -Only Condition. To isolate the contribution of changes in electrical potential within the synaptic cleft to NQT, we held ion concentrations in the synaptic cleft constant at 5 mM for $[K^+]_{SC}$ and 140 mM $[Na^+]_{SC}$ (Eqs. S3 and S4) and removed terms for ion diffusion in the cleft from Eq. S5.

$$(2C_m) \frac{d\phi_{SC}}{dt} = C_m \frac{d\phi_H}{dt} + C_m \frac{d\phi_C}{dt} + J_H + J_{CIF} + \nabla \cdot \left(\left(\sigma_{O_{SC}} + \frac{D_K [K^+]_{SC} F^2}{RT} + \frac{D_{Na} [Na^+]_{SC} F^2}{RT} \right) \nabla \phi_{SC} \right) \cdot d_{SC} \quad (S8)$$

$$\frac{\partial [K^+]_{SC}}{\partial t} = 0; [K^+]_{SC} = 5 \text{ mM} \quad (S9)$$

$$\frac{\partial [Na^+]_{SC}}{\partial t} = 0; [Na^+]_{SC} = 140 \text{ mM} \quad (S10)$$

$[K^+]_{SC}$ -Only Condition. To isolate the contribution of changes in K^+ concentration in the synaptic cleft to NQT, we fixed ϕ_{SC} at 0 mV and removed the electrical drift terms in Eqs. S3 and S4.

$$(2C_m) \frac{d\phi_{SC}}{dt} = 0; \phi_{SC} = 0 \text{ mV} \quad (S11)$$

$$\frac{\partial [K^+]_{SC}}{\partial t} = \nabla \cdot (D_K \nabla [K^+]_{SC}) + \frac{1}{d_{SC}} \frac{(J_{KH} + J_{K CIF})}{F} \quad (S12)$$

$$\frac{\partial [Na^+]_{SC}}{\partial t} = \nabla \cdot (D_{Na} \nabla [Na^+]_{SC}) + \frac{1}{d_{SC}} \frac{(J_{NaH} + J_{Na CIF})}{F} \quad (S13)$$

Model Simulation and Solver Conditions

In the COMSOL 5.6 software, the finite element mesh was generated based on geometric parameters for the hair cell-calyx and fiber ([Fig. S1](#)). The number and distribution of finite element nodes (hair cell-calyx: 26 nodes, 25 edge elements; fiber: 95 nodes, 94 edge elements) was chosen to minimize error in the solutions of the governing equations. To obtain the resting conditions, we ran the model simulation with a stationary solver. For a step or sinusoidal displacement of the hair cell's stereociliary bundle or hair cell voltage steps, we used a time-dependent solver to determine the responses in the hair cell, synaptic cleft, calyx, and afferent fiber.

For step stimuli, the specified output time ranges were 0:1:49; 49:0.1:50; 50:0.01:60; 60:0.1:500. In this notation, the middle value indicates the increment between the time values (in ms) on either side. For sinusoidal stimuli ([Fig. 5](#)) the increment was 0.1 ms and the duration of the simulation was adjusted to match the length of the stimulus taken from Songer and Eatock (2013). The time dependent solver in COMSOL utilizes adaptive time stepping which is also affected by an error tolerance setting within the software. A relative tolerance of 1E-4 was used. The solver has multiple settings which control aspects of adaptive time stepping and how solver time steps are taken in relation to the specified output times. Results are interpolated where solver time steps do not exactly coincide with specified output times. We first used the 'strict' setting which ensures a step is taken at each specified output time. This produced results consistent with the 'free' setting where the solver dynamically takes smaller or larger steps while satisfying tolerances. We subsequently used the 'free' setting for our simulations as it reduced computation time and memory requirements. Enforcing smaller time steps for the full duration of the simulation did not significantly alter the computed results. The time-dependent solver was run using the backward difference formula (BDF) method.

The model simultaneously solves [Eqs. S1-S7](#) to simulate the electrical potential of the hair cell and the spatiotemporal evolution of electrical potential, potassium concentration, sodium concentration in the synaptic cleft, and potential in the afferent fiber.

Table S5 – Conductances, Diffusion Coefficients and Capacitances

σ_C	1000 nS/ μm	Baumann et al. 1997; Geddes and Baker 1967; Zhou et al. 2016; Wang et al. 2017
C_m	0.01 pF/ μm^2	Curtis and Cole 1938; Hodgkin and Huxley 1952*
$C_{m,Myel}$	0.00002 pF/ μm^2	Stämpfli 1954
D_K	0.81 $\mu\text{m}/\text{ms}$	Lide 2005. See methods near Eq. S4
D_{Na}	0.56 $\mu\text{m}/\text{ms}$	Lide 2005. See methods near Eq. S4
$g_{bundle,max}$	5 nS	Holt et al. 1997
$g_{Ca,max}$	0.5 nS	Bao et al. 2003
$g_{HCN1,max}$	4.2 nS	Horwitz et al. 2011
$g_{HCN2,max}$	3.6 nS	Horwitz et al. 2014
$g_{K,L,max}$	80 nS	Spaiardi et al. 2017
$g_{K_V7.4,max}$	24 nS	Hurley et al. 2006
$g_{K_V1.x,max}$	6.3 nS	Kalluri et al. 2010
$G_{K_V3.4,max}$	0.2 nS/ μm^2	Chabbert et al. 2001
$g_{K_V7.x,max}$	4.5 nS	Kalluri et al. 2010
$g_{Na_V,unitary}$	10 pS	Bezanilla 1987; Kay et al. 1998
ρ_{Na_V}	12,000/ μm^2	Ritchie and Rogart 1977

*Reported C_m values vary between 0.008 to 0.015 pF/ μm^2 ; we use 0.01 pF/ μm^2 .

Also see: Gentet et al. (2000) which summarizes measurements of specific capacitance in various cells.

Channel Distribution and Kinetics

The governing equations depend upon the net current densities across the pre- and post-synaptic membranes in the model. The constitutive currents and their kinetics as used in the model are detailed in **Table S6**. All channel properties used were from electrophysiological measurements near room temperature (23 – 27°C). For a given channel, $act_{\infty}(V)$ and $\tau_{act}(V)$ are expressions for the dependence of the activation ‘act’ (or inactivation ‘inact’) gating variable on the membrane voltage and the corresponding time constant. $act(t)$ is the instantaneous value of the gating variable. The expressions for $act(V)$ and $\tau_{act}(V)$ were stored in variables assigned to the VHCC and fiber geometry to make them locally available during model evaluation. The maximum whole-cell conductance value $g_{x,max}$ for any type of channel ‘x’ was divided by the surface area to obtain the maximum conductance density $G_{x,max}$ to allow us to evaluate local current densities at specific sites in the model. The transporters Na⁺/K⁺-ATPase and KCC were assumed to operate at pseudo-steady state and depend only on extracellular [K⁺]. On the hair cell, basolateral channels were only distributed to the part of the membrane enclosed by the calyx, consistent with immunolocalization data (Lysakowski et al. 2011).

Table S6. Current Densities and Kinetics

MET (Hair Cell Apical)

$$I(X) = g_{bundle,max} \cdot P_{MET} \cdot (\phi_H - V_{bundle,rev} - \phi_{endolymph})$$

$$P_{MET} = \left(1 + \exp\left(4.05 \cdot \left(0.39 - \frac{X+200}{1000}\right)\right)\right)^{-1} \cdot \left(1 + \exp\left(14.5 \cdot \left(0.25 - \frac{X+200}{1000}\right)\right)\right)^{-1}$$

$X = displacement(t)$; Step or sinusoidal functions were used.

Kinetics: (Holt et al. 1997).

$V_{bundle,rev}$, the reversal voltage: 0 mV (Corns et al. 2014).

$\phi_{endolymph}$, the endolymphatic potential: 5 mV (Köppl et al. 2018; Li et al. 2020).

g_{K,L} (Hair Cell)

$$J_{K,L} = G_{K,L,max} \cdot P_{K,L} \cdot (V_m - E_K)$$

$$G_{K,L,max} = \frac{g_{K,L,max}}{a_{H,C}}$$

$$P_{K,L} = act_{K,L}$$

$$\tau_{K,L} \cdot \frac{d(act_{K,L})}{dt} = act_{\infty,K,L} - act_{K,L}$$

$$\tau_{K,L} = 429.7 \cdot \exp\left(-0.2826 \cdot \frac{V_m - (-80)}{2.84}\right) + 10$$

$$act_{\infty,K,L} = \left(1 + \exp\left(-\frac{V_m - (-80)}{2.84}\right) \right)^{-1}$$

Presence in hair cell: (Rennie and Correia 1994; Rüscher and Eatock 1996).

Activation Kinetics in the model: (Spaiardi et al. 2017, 2020).

$\tau_{K,L}$ is based on measurements of the slow time constant: (Wong et al. 2004; Songer and Eatock 2013; Spaiardi et al. 2017).

g_{Ca} (Hair Cell)

$$J_{Ca} = G_{Ca,max} \cdot P_{Ca} \cdot (V_m - E_{Ca})$$

$$G_{Ca,max} = g_{Ca,max} / a_{H,C}$$

$$P_{Ca} = act_{Ca}$$

$$\tau_{Ca} \cdot \frac{d(act_{Ca})}{dt} = act_{\infty,Ca} - act_{Ca}$$

$$\tau_{Ca} = 0.6 \text{ ms}$$

$$act_{\infty,Ca} = \frac{1}{1 + \exp\left(-\frac{V_m - (-44)}{5.8}\right)}$$

Presence and Kinetics: (Bao et al. 2003), assuming an intracellular $[Ca^{2+}]$ of $1 \mu M$ lower than estimated for synaptic zone Ca^{2+} concentration in frog saccular hair cells, which have much larger Ca^{2+} currents at resting potential (Roberts et al. 1991).

H_{CN1} (Hair Cell)

$$J_{K,HCN1} = \frac{4}{5} \cdot G_{HCN1,max} \cdot P_{HCN1} \cdot (V_m - E_K)$$

$$J_{Na,HCN1} = \frac{1}{5} \cdot G_{HCN1,max} \cdot P_{HCN1} \cdot (V_m - E_{Na})$$

$$G_{HCN1,max} = g_{HCN1,max} / a_{H,C}$$

$$P_{HCN1} = act_{HCN1}$$

$$\tau_{HCN1} \cdot \frac{d(A_{HCN1})}{dt} = act_{\infty,HCN1} - act_{HCN1}$$

$$\tau_{HCN1} = 209.479 + \frac{\left(\exp\left(-\frac{V_m + 80.646}{6.916}\right) \right)^{-1} + \exp\left(\frac{V_m + 80.646}{14.881}\right)}{2551.988}$$

$$act_{\infty,HCN1} = \frac{1}{1 + \exp\left(\frac{V_m - (-90)}{6.8}\right)}$$

Location and Kinetics: (Horwitz et al. 2011).

τ_{HCN1} : (Ventura and Kalluri 2019), Parameters for the HCN “Max Activation” case. These parameters were for I_H in rat vestibular ganglion neurons, no distinction was made between HCN1 vs HCN2. We assume the time constants are similar.

The $K^+ : Na^+$ permeability ratio through HCN1 channels is 4:1 (Lee and MacKinnon 2017). The fractions 4/5 and 1/5 in the equations for $J_{K,HCN1}$, and $J_{Na,HCN1}$ reflect this.

Na⁺/K⁺-ATPase (Hair Cell | Calyx Inner Face | Calyx Outer Face)

$$J_{pump} = (3 - 2) \cdot \frac{F \cdot 10^{12}}{N_A} \cdot \rho_{NaK} \cdot v_{NaK} \cdot P_{pump}$$

$$\rho_{NaK} = 1000 \mid 1000 \mid 2000 \text{ pumps}/\mu\text{m}^2$$

$$P_{pump} = \left(\frac{[K^+]_{SC}}{[K^+]_{SC+1.5}} \right)^2 \mid \left(\frac{[K^+]_{SC}}{[K^+]_{SC+1.5}} \right)^2 \mid \left(\frac{5}{5+1.5} \right)^2 ;$$

Presence of Na⁺/K⁺-ATPase: (Schuth et al. 2014).

A pseudo-steady state expression was used with v_{NaK} of 100/s, a Hill coefficient of 2 (Jaisser et al. 1994) and a K⁺ molar affinity of 1.5 mM, adapted from (Crambert et al. 2000). ρ_{NaK} values were chosen such that the $[Na^+]_{SC}$ at rest, at the base of the cleft, was between 120 – 140 mM with the reasoning that quantal currents occurring at the calyx inner face would require sufficient Na⁺ driving forces. In the expression for J_{pump} , 10^{12} is a conversion factor from Coulombs to picoCoulombs. P_{pump} is a simplified expression of pump activity as a function of external $[K^+]$ and the molar affinity of K⁺.

KCC4 (Calyx Inner Face)

$$J_{KCC4} = J_{KCC4,max} \cdot P_{KCC4}$$

$$J_{KCC4,max} = 2 \text{ pA}/\mu\text{m}^2$$

$$P_{KCC4} = \left(1 + \left(\frac{17.5}{[K^+]_{SC}} \right)^2 \right)^{-1}$$

Molar affinity (17.5 mM) from (Mercado et al. 2000). Hill Coefficient based on discussions in (Marcoux et al. 2017). $J_{KCC4,max}$ was chosen such that the $[K^+]_{SC}$ at rest, at the base of the cleft as calculated by the stationary solver was between 5-7 mM. Although J_{KCC4} is expressed as a current, transport activity of KCC is electroneutral and does not contribute to a change in potential. KCC4 was localized to the calyx inner face, see [Experimental Methods](#).

K_V7.4 (Calyx Inner Face | Calyx Outer Face)

$$J_{KV7.4} = G_{KV7.4,max} \cdot P_{KV7.4} \cdot (V_m - E_K)$$

$$G_{KV7.4,max} = \frac{\frac{4}{5} g_{KV7.4,max}}{a_{CIF}} \mid \frac{\frac{1}{5} g_{KV7.4,max}}{a_{COF}}$$

$$P_{KV7.4} = act_{KV7.4}$$

$$\tau_{KV7.4} \cdot \frac{d(act_{KV7.4})}{dt} = act_{\infty,KV7.4} - act_{KV7.4}$$

$$\tau_{KV7.4} = \max((0.0002488 \cdot \exp(-0.04401 \cdot V_m) + 0.4506 \cdot \exp(0.05437 \cdot V_m))^{-1}, 1)$$

$$act_{\infty, KV7.4} = \left(1 + \exp\left(\frac{V_m - (-52)}{16}\right)\right)^{-1}$$

Location & Kinetics: (Hurley et al. 2006).

In $G_{KV7.4, max}$, the fractions 4/5 and 1/5 reflect the relative density of the channel on either membrane observed in electron microscope immunogold experiments. See [Experimental Methods](#).

HCN2 (Calyx Inner Face | Calyx Outer Face)

$$J_{K, HCN2} = \frac{4}{5} \cdot G_{HCN2, max} \cdot P_{HCN2} \cdot (V_m - E_K)$$

$$J_{Na, HCN2} = \frac{1}{5} \cdot G_{HCN2, max} \cdot P_{HCN2} \cdot (V_m - E_{Na})$$

$$G_{HCN2, max} = \frac{\frac{1}{2} g_{HCN2, max}}{a_{CIF}} \mid \frac{\frac{1}{2} g_{HCN2, max}}{a_{COF}} \quad g_{HCN2, max} \text{ was distributed equally to both the CIF and COF.}$$

$$P_{HCN2} = act_{HCN2}$$

$$\tau_{HCN2} \frac{d(act_{HCN2})}{dt} = act_{\infty, HCN2} - act_{HCN2}$$

$$\tau_{HCN2} = 209.479 + \left(\left(\exp\left(-\frac{V_m + 80.646}{6.916}\right) \right)^{-1} + \exp\left(\frac{V_m + 80.646}{14.881}\right) \right) / 2551.988$$

$$act_{\infty, HCN2} = \left(1 + \exp\left(\frac{V_m + 95}{11.7}\right)\right)^{-1}$$

Presence and Kinetics: (Horwitz et al. 2014). Adapted for a simple calyx.

τ_{HCN2} : (Ventura and Kalluri 2019), Parameters for the HCN “Max Activation” case.

The $K^+ : Na^+$ Permeability ratio through HCN1 channels is 4:1 (Lee and MacKinnon 2017). The same ratio was assumed for HCN2 channels. The fractions 4/5 and 1/5 in the equations for $J_{K, HCN2}$, and $J_{Na, HCN2}$ reflect this.

I_{Leak} (Calyx Outer Face)

$$J_{Leak} = G_{Leak, max} \cdot (V_m - 0)$$

$$G_{Leak, max} = \frac{g_{Leak, max}}{a_{COF}}$$

$g_{Leak, max}$ was set equal to 2 nS. The value was chosen to compensate for unknown membrane properties and assist in setting the resting calyx potential.

K_v7.x (Hemi-Node | Node)

$$J_{K_V7.x} = G_{K_V7.x,max} \cdot P_{K_V7.x} \cdot (V_m - E_k)$$

$$G_{K_V7.x,max} = \frac{g_{K_V7.x,max}}{a_{F,HN} + 2a_{F,N}}$$

$$P_{K_V7.x} = act_{K_V7.x}$$

$$\tau_{K_V7.x} \cdot \frac{d(act_{K_V7.x})}{dt} = act_{\infty,K_V7.x} - act_{K_V7.x}$$

$$\tau_{K_V7.x} = 1.2 \cdot \exp(-0.08 \cdot V_m) \cdot \frac{1}{1 + \exp\left(-\frac{V_m + 47}{8}\right)}$$

$$act_{\infty,K_V7.x} = \frac{1}{1 + \exp\left(-\frac{V_m + 47}{8}\right)}$$

Kinetics: (Kalluri et al. 2010).

K_v3.4 (Hemi-Node | Node)

$$J_{K_V3.4} = G_{K_V3.4,max} \cdot P_{K_V3.4} \cdot (V_m - E_k)$$

$$P_{K_V3.4} = act_{K_V3.4} \cdot inact_{K_V3.4}$$

$$\tau_{K_V3.4,act} \cdot \frac{d(act_{K_V3.4})}{dt} = act_{\infty,K_V3.4} - act_{K_V3.4}$$

$$\tau_{K_V3.4,inact} \cdot \frac{d(inact_{K_V3.4})}{dt} = inact_{\infty,K_V3.4} - inact_{K_V3.4}$$

$$\tau_{K_V3.4,act} = 5 \cdot 1.41 \cdot \exp(-0.05589 \cdot V_m) \cdot \left(1 + \exp\left(-\frac{V_m + 31.3}{8.5}\right)\right)^{-1}$$

$$\tau_{K_V3.4,inact} = 25.4 \text{ ms}$$

$$act_{\infty,K_V3.4} = \left(1 + \exp\left(-\frac{V_m + 31.3}{8.5}\right)\right)^{-1}$$

$$inact_{\infty,K_V3.4} = \left(1 + \exp\left(\frac{V_m + 65.84}{5.51}\right)\right)^{-1}$$

Kinetics: (Chabbert et al. 2001). $G_{K_V3.4,max}$ was adapted to a value of 0.2 nS/ μm^2 and is comparable to the values for $G_{K_V1.x,max}$ and $G_{K_V7.x,max}$.

K_v1.x (Hemi-Node | Node)

$$J_{K_V1} = G_{K_V1,max} \cdot P_{K_V1} \cdot (V_m - E_k)$$

$$G_{K_V1.x,max} = \frac{g_{K_V1.x,max}}{a_{F,HN} + 2a_{F,N}}$$

$$P_{K_V1} = act_{K_V1}$$

$$\tau_{K_V1} \cdot \frac{d(act_{K_V1})}{dt} = act_{\infty,K_V1} - act_{K_V1}$$

$$act_{\infty,K_V1} = \frac{1}{1 + \exp\left(-\frac{V_m + 44}{7.1}\right)}$$

$$\tau_{KV1} = 3.7 \text{ ms}$$

Kinetics: (Kalluri et al. 2010).

Na_v (Unmyelinated | Hemi-Node | Node)

$$J_{NaV} = G_{NaV,max} \cdot P_{NaV} \cdot (V_m - E_{Na})$$

$$J_{NaV,Unmyel} = \frac{1}{4} \cdot G_{NaV,max} \cdot P_{NaV} \cdot (V_m - E_{Na})$$

$$G_{NaV,max} = g_{NaV,unitary} \cdot \rho_{NaV}$$

$$P_{NaV} = act_{NaV} \cdot inact_{NaV}$$

$$\tau_{NaV,act} \cdot \frac{d(act_{NaV})}{dt} = act_{\infty,NaV} - act_{NaV}$$

$$\tau_{NaV,inact} \cdot \frac{d(inact_{NaV})}{dt} = inact_{\infty,NaV} - inact_{NaV}$$

$$\tau_{NaV,act} = \left(1 + \exp\left(-\frac{V_m + 41.58}{5.733}\right)\right)^{-1} \cdot \left(1 + \exp\left(\frac{V_m + 8.295}{16.28}\right)\right)^{-1} + 0.2$$

(for $-55 \leq V_m \leq 60 \text{ mV}$); 0.2 ms otherwise.

$$\tau_{NaV,inact} = 0.0001452 \exp(-0.2211 V_m) + 0.2382$$

(for $-45 \leq V_m \leq 60 \text{ mV}$); else, linearly extrapolated.

$$act_{\infty,NaV} = \left(1 + \exp\left(-\frac{V_m + 40}{8}\right)\right)^{-1}$$

$$inact_{\infty,NaV} = \left(1 + \exp\left(\frac{V_m + 69}{7.6}\right)\right)^{-1}$$

Kinetics: (Liu et al. 2016; Meredith and Rennie 2018).

$\tau_{NaV,act}$ and $\tau_{NaV,inact}$, see [Experimental Methods](#).

A reduced channel density was assumed at the unmyelinated segment and the maximum conductance density reduced to $\frac{1}{4}$ of the full value. This reflects evidence for greater channel clustering near regions adjacent to myelinated segments of fiber (Freeman et al. 2016).

Table S7 - Sources

Model Compartment	Property	Reference	Animal	Location	Age
General	Calyx Dimensions	Lysakowski et al. 2011 Fig. 2C – central calyx-only afferent	Rat	SCC	6 Months
Hair Cell	MET	Holt et al. 1997	Mouse	Utricle	P1 - P10
	MET, P ₀ = 10%	Songer and Eatock 2013	Rat	Saccule	P1 - P9
	MET, 5nS	Holt et al. 1997	Mouse	Utricle	P1 - P10
	$g_{K,L}$	Spaiardi et al. 2017	Mouse	SCC	P6 - P19
	$\tau_{g_{K,L}}$	Wong et al. 2004	Rat	Utricle	P16 - P24
	Fit of slow time constant	Songer and Eatock 2013	Rat	Saccule	P1 – P9
		Spaiardi et al. 2017	Mouse	SCC	P6 - P19
		g_{Ca}	Bao et al. 2003	Rat	SCC
	HCN1	Horwitz et al. 2011	Mouse	Utricle	P0 - P25
HC/Calyx	Na ⁺ /K ⁺ -ATPase	Schuth et al. 2014	Rat	Utricle/SCC	P17– P25
	τ_{HCN}	Ventura and Kalluri 2019 - HCN Max Activation parameters	Rat	VGN	P9 - P21
Calyx	HCN2	Horwitz et al. 2014	Mouse	Utricle	P0 - P25
	K _v 7.4	Hurley et al. 2006	Rat	Utricle	P2 - P26
		Lysakowski et al. 2011	Rat	Utricle/SCC	6 Months
	KCC4	See Experimental Methods	Rat	SCC	6 months
		Mercado et al. 2000	Frog oocyte (expressing mouse KCC4)	-	Day 5
	Marcoux et al. 2017	Various mammals	-	-	
Fiber	HN, N1 Location	Lysakowski et al. 2011	Rat	Utricle, Saccule and SCC	6 Months

Na _v	Liu et al. 2016	Rat	VGN	P1 - P8
	Meredith and Rennie 2018	Gerbil	SCC	P5 - P31
K _{v7}	Kalluri et al. 2010	Rat	VGN	P8 - P15
K _{v1}	Kalluri et al. 2010	Rat	VGN	P8 - P15
K _{v3.4}	Chabbert et al. 2001	Mouse	VGN	P5 - P8

SCC – Semicircular Canal Crista. Utricle and saccule reference their maculae. Conductance values are presented in [Table S5](#) and kinetics are presented in [Table S6](#).

Additional Sources

The following were not used in this iteration of the model, but we include them for readers of this supplement.

HCN Kinetics – Gerbil (Meredith et al. 2012)

$g_{K,L}$ – Turtle (Brichta et al. 2002)

$g_{K,L}$ – Mouse - (Rüsch and Eatock 1996)

Notes

Model Repository: <https://github.com/acgsci/vestibularHairCellCalyxNQT>

Width of the synaptic cleft

Previously, a phenomenological cleft width of ~ 67 nm was derived using measurements of E_K across the hair cell membrane and a multi-compartment model that related the rise time of cleft potassium to cleft width (Lim et al. 2011). This value differs more than 3-fold from that measured in EM studies: ~ 20 nm (Spoendlin 1966). Accepted fixation shrinkage in EM preparations is $\sim 15\%$. Correspondingly, cryo-fixed material that does not involve sample dehydration reports cleft widths of 23-35 nm (Korogod et al. 2015)

Ions needed to change E_K vs. V_m

The number of ions necessary to alter E_K is typically greater than the number of uncompensated charges required to effect an equivalent change in V_m . For example, assuming a uniform 5 mM of K^+ in the modelled synaptic cleft ($\sim 6 \mu\text{m}^3$ in volume), and 150 mM K^+ in the hair cell ($\sim 600 \mu\text{m}^3$ in volume), increasing E_K by 1 mV requires a ~ 0.2 mM increase in cleft K^+ concentration or $\sim 720,000$ K^+ ions. E_K also changes non-linearly such that more K^+ ions are required as the cleft K^+ concentration increases. In comparison, increasing the voltage of the hair cell membrane facing the cleft ($\sim 300 \mu\text{m}^2$; $C_m = 0.01 \text{ pF}/\mu\text{m}^2$) by 1 mV requires $\sim 19,000$ uncompensated charges. Similarly, considering the cleft as a compartment bounded by the hair cell and calyx inner face membranes ($\sim 600 \mu\text{m}^2$) increasing its potential by 1 mV requires $\sim 38,000$ uncompensated charges.

Effects of external $[K^+]$ on $g_{K,L}$

Prior data on the rodent VHCC (our model preparation; see Fig. 4, Rüsçh and Eatock, 1996) demonstrates an increase in $g_{K,L}$ with increased external K^+ . This change in conductance with $[K^+]$ is well explained by the Goldman-Hodgkin-Katz (GHK) Flux equation. We used [Eq. S1](#) to describe currents in the model as most of our sources report channel conductances, not permeabilities. Upon replacing the current equation for $g_{K,L}$ in the model with the GHK equation obtained by Rüsçh and Eatock, we found that the effects on model results were small (2 mV depolarization of resting hair cell potential and maximal depolarization during bundle displacement).

' K^+ Relief of Block' (KRB) Model

Contini et al. (2020) proposed that the activity of $g_{K,L}$ can be explained by potassium relief of block. Their KRB model involves a number of parameters, including the concentration of the blocking particle over the half blocking dose (B), the voltage at half-maximal block (V_B), and the voltage dependence of the block (V_e). These parameters were presented in relation to external $[K^+]$ of 4 mM and 20 mM K^+ . To evaluate how the KRB model of $g_{K,L}$ alters VHCC model predictions, we linearly extrapolated the above parameters as functions of concentration using the 4 mM and 20 mM datapoints. We then modified the activation curve of $g_{K,L}$ as follows :

$$act_{\infty,K,L} = \left(1 + B \exp\left(-\frac{V_m - V_B}{V_e}\right) \right)^{-1} \quad (\text{S14})$$

V_m is V_H , the hair cell membrane voltage. For + 1- μm step bundle displacement, modifying the $g_{K,L}$ activation curve to include KRB had small effects: decreases of $\sim 10\text{-}25$ pA in resting and steady state $g_{K,L}$ currents, and $\sim 3\text{-}4$ mV more positive hair cell resting potential and steady-state receptor potential. With the KRB activation curve, $g_{K,L}$ open probabilities were enhanced at the base and reduced at the apex of the cleft following the gradient in cleft $[\text{K}^+]$.

We performed preliminary simulations to evaluate the influence of KRB on NQT. For the sinusoidal displacement stimulus of **Fig. 5**, using the KRB model (1) had minor effects on the amplitude and phase of the simulated calyx postsynaptic potentials (**Fig. S4**); (2) did not affect our conclusion that fast NQT at voltage step onset is mediated by changes in cleft electrical potential.

In summary, the KRB model produces results comparable with previous descriptions of $g_{K,L}$ over the physiological range of hair cell operation, with the added benefit of explaining data under large voltage excursions at high potassium concentrations.

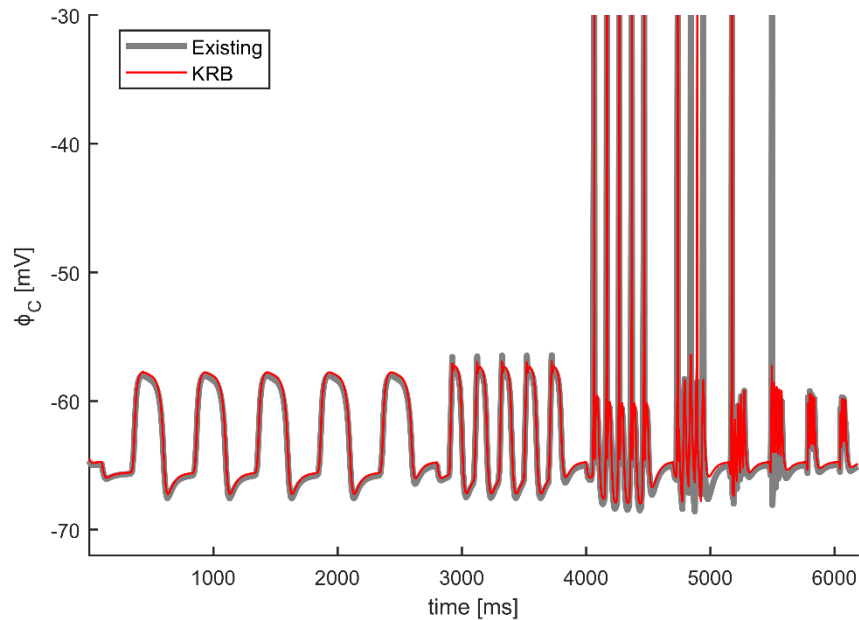


Fig. S4 – Comparison of post-synaptic depolarization during sinusoidal bundle displacement with the existing and KRB activation curves of $g_{K,L}$.

The predicted responses to bundle stimulation modeled in Figure 5A in the manuscript (grey) using the description of $g_{K,L}$ ([Table S6](#)) is overlaid by the simulated response when $g_{K,L}$ steady-state activation is described by KRB ([Eq. S14](#)).

Effect of Series Resistance on Fast Postsynaptic Currents

In the main text, in **Figure 6**, we simulated an ideal voltage clamp to control the intracellular potentials of the hair cell and calyx. Here, we present the effect of including a series resistance of $5\text{ M}\Omega$ - the value after 65% compensation of $15\text{ M}\Omega$, the maximal series resistance reported in Contini et al. (2020). In **Table S8** we show the effect of adding series resistance on hair cell intracellular potential (ϕ_H), the cleft electrical potential (ϕ_{SC}) and membrane voltage of the calyx inner face (V_{CIF}). At the -70 mV holding potential (green, **Fig. S5**), series resistance effects will reduce the cleft electrical potential by 10 mV , from 54 to 44 mV (**Table S8**), and slightly reduce the fast post-synaptic currents (**Fig. S5, middle**). Simulating the series resistance and using the [KRB model of \$g_{K,L}\$](#) resulted in a further decrease (**Fig. S5, right**) coming closer to the data recorded by Contini et al. (2020).

Table S8. Effect of Series Resistance on Cleft Electrical Potential and Membrane Voltages.

Holding condition	ϕ_H , mV		ϕ_{SC} , mV		V_{CIF} , mV	
	<i>Ideal</i>	$+R_S$	<i>Ideal</i>	$+R_S$	<i>Ideal</i>	$+R_S$
-100 (t=50.05 ms)	20	-8.5	41.4	41.3	-141.4	-139.8
-70 (t=50.1 ms)	20	2.7	54.7	44.8	-124.7	-113.6

$R_S = 5\text{ M}\Omega$; Values are at the time of peak $I_{CIF,R}$ following steps to 20 mV from the given holding potential.

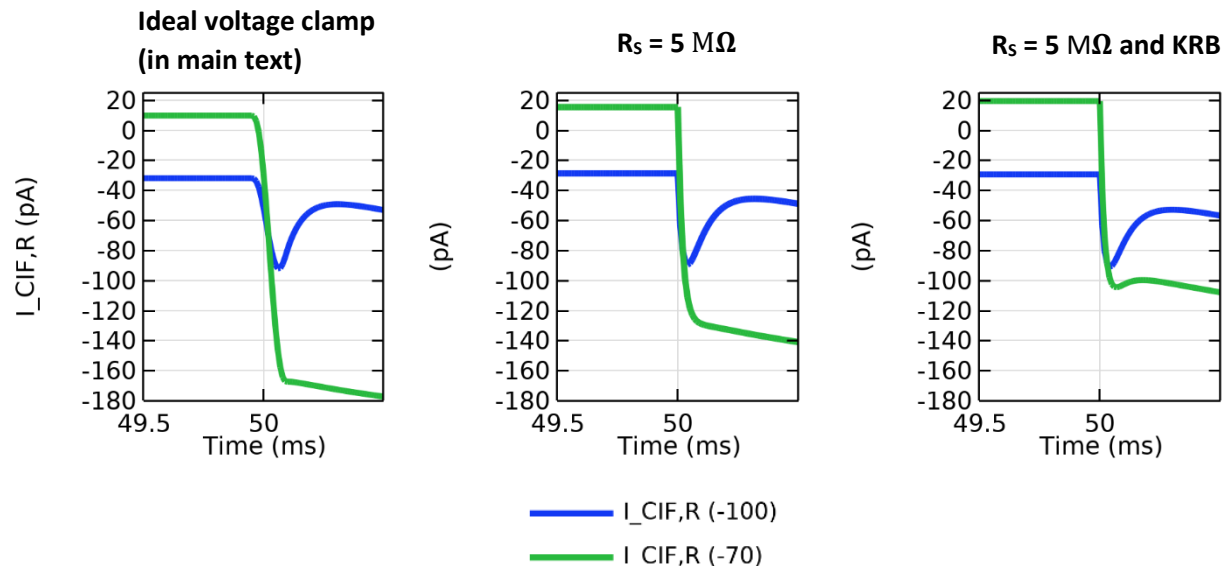


Fig. S5 – Effects of series resistance and KRB on fast post synaptic currents.

Fast post-synaptic resistive currents ($I_{CIF,R}$) are shown in response to voltage steps to 20 mV from holding potentials of -100 mV (blue) and -70 mV (green) for the ideal voltage clamp simulated in Figure 6 (left), voltage clamp with series resistance of $R_S = 5\text{ M}\Omega$ (middle) and with both $R_S = 5\text{ M}\Omega$ and KRB (right).

Experimental Methods

Below we describe the experimental methods used to determine some parameters listed in the Tables, and imaged cells shown in **Fig. 1A**.

Na_v time constants ([Table S6](#)):

Whole-cell patch clamp recordings from mouse vestibular afferent neurons. The kinetics of postsynaptic (afferent) Na_v currents were obtained from mouse vestibular ganglion neurons isolated in the first postnatal month. Animals were handled in accordance with the *National Institutes of Health Guide for the Care and Use of Laboratory Animals*, and all procedures were approved by the animal care committee at the University of Chicago. Mice were deeply anesthetized with isoflurane and decapitated. Vestibular ganglia were dissected out and mechanically dissociated following enzymatic digestion (with 0.12% collagenase and 0.12% trypsin for 15-20 minutes at 37°C) and cultured overnight to remove satellite cells, in minimal essential medium with Glutamax (MEM, Invitrogen, Carlsbad, CA) supplemented with 10 mM HEPES, 5% fetal bovine serum (FBS), and 1% penicillin in 5% CO₂-95% air at 37°C. Whole-cell patch clamp recordings were made with solutions designed to minimize contamination from K⁺ and Ca²⁺ currents. The external medium comprised (mM): 75 NaCl, 5.4 CsCl, 2.5 MgCl₂, 75 TEA Cl, 5 HEPES, 10 D-glucose, titrated with CsOH to pH 7.4, with osmolality ~310 mmol/kg. The internal (pipette) solution contained: 148 CsCl, 0.8 CaCl, 3.5 Na₂-creatine phosphate, 3.5 MgATP, 0.1 LiGTP, 5 EGTA, 5 HEPES, 0.1 Na-cAMP, titrated with CsOH to pH 7.4, and ~300 mmol/kg. Recordings were made at room temperature (23-25°C). Signals were delivered and recorded with a Multiclamp 700B amplifier, Digidata 1440A digitizer, and pClamp 10 or 11 software (Axon Instruments, Molecular Devices, Sunnyvale, CA), with low-pass Bessel filtering set at 10 kHz and sampling interval set at 5 μs. Seal resistance exceeded 1 GΩ. Membrane voltages were corrected off-line for a measured liquid junction potential of 6.4 mV and for series resistance errors. Analysis was performed with MATLAB (The MathWorks, Natick, MA), Clampfit (Axon Instruments, Molecular Devices), and Origin Pro 2018 (OriginLab, Northampton, MA). Series resistance (R_s) ranged between 3 and 10 MΩ and was compensated by 75%. The holding potential was -66.4 mV. Activation and inactivation time courses were measured for currents evoked by depolarizing voltage steps following a pre-pulse to -127 mV to de-inactivate Na_v current. The currents were fit with the following Hodgkin-Huxley equations for Na_v channel activation (n=6) and inactivation (n=9):

$$I(t) = I_{peak} \left(1 - e^{-\frac{t}{\tau_m}}\right)^3 ; I(t) = I_{SS} + I_{peak}(e^{-t/\tau_h})$$

where I is current, t is time; I_{peak} and I_f are peak and steady-state (inactivated) currents, respectively; and τ_m and τ_h are the time constants for the activation and inactivation transitions, respectively.

**Location of KCC, relative density of Kv7.4 (Table S6) and image of hair cells and calyces (Fig. 1A):
Confocal microscopy and immunocytochemistry**

Fixation. Animals were handled in accordance with the *National Institutes of Health Guide for the Care and Use of Laboratory Animals*, and all procedures were approved by the IACUC at the Univ. of Illinois at Chicago. Long-Evans rats (Charles River Laboratories, Wilmington, MA) were deeply anesthetized with Nembutal (80 mg/kg), then perfused transcardially for 1 min with physiological saline containing heparin (2000 IU), followed by a dialdehyde fixative for 10 min (4% paraformaldehyde, 1% acrolein, 1% picric acid, and 5% sucrose in 0.1 M phosphate buffer (PB), pH 7.4). After decapitation, the head was post-fixed in the fixative for 20 min and then placed in 30% sucrose in 0.1 M PB. Vestibular and auditory organs were dissected out with the head immersed in PB. Decalcification of cochleas and removal of bone debris and otoliths from vestibular organs was accomplished through incubation in Cal-X solution. Background fluorescence was reduced by incubating the tissues in a 1% aqueous solution of sodium borohydride for 10 min. All organs were then placed in 30% sucrose in 0.1 M PB overnight.

Immunohistochemistry. Dissected tissues were gelatin-embedded and cut with a freezing sliding microtome. Tissue permeabilization was carried out with 4% Triton X-100 in PBS for 1 hr, and a blocking solution composed of 0.5% fish gelatin, 0.5% Triton X-100 and 1% BSA in 10 mM phosphate-buffered saline (PBS) was used for 1 hr. Samples were incubated in primary antibodies diluted 1:200 in blocking solution: goat anti-calretinin (AB1550), rabbit anti-KCC4 (AB3270) (all available or formerly available from Chemicon/Millipore-Sigma, St. Louis, MO) or rabbit anti-myosin 6 (a generous gift from Dr. Tama Hasson). The anti-calretinin antibody served as a marker of type II hair cells and calyx afferents (Desai et al. 2005). Specific labeling was revealed with these secondary antibodies (1:200 in the blocking solution): FITC-conjugated donkey anti-goat and rhodamine-conjugated donkey anti-rabbit (both from Chemicon, Temecula, CA). Sections were mounted on slides using a medium containing Mowiol (Calbiochem, Darmstadt, Germany) and examined on a confocal microscope (LSM 510 META, Carl Zeiss, Oberkochen, Germany). The relative density of Kv7.4 channels was based on electron microscopic (EM) immunogold experiments, with methods described in Hurley et al. (2006). In brief, 40- μ m vibratome sections were incubated in primary antibody [1:200 rabbit anti-KCNQ4, a generous gift from Dr. Bechara Kachar] for 72 h and secondary antibody (1:50; colloidal gold-labeled goat anti-rabbit IgG; Amersham Biosciences, Piscataway, NJ) for 24 h. Colloidal gold staining was silver-enhanced (4–8 min; IntenSE M kit; Amersham Biosciences). For more details, see Hurley et al. (2006).

SI References

Bao H, Wong WH, Goldberg JM, Eatock RA. Voltage-gated calcium channel currents in type I and type II hair cells isolated from the rat crista. *J Neurophysiol* 90: 155–164, 2003.

Baumann SB, Wozny DR, Kelly SK, Meno FM. The electrical conductivity of human cerebrospinal fluid at body temperature. *IEEE Trans Biomed Eng* 44: 220–223, 1997.

Bezanilla F. Single sodium channels from the squid giant axon. *Biophys J* 52: 1087–1090, 1987.

Brichta AM, Aubert A, Eatock RA, Goldberg JM. Regional analysis of whole cell currents from hair cells of the turtle posterior crista. *J Neurophysiol* 88: 3259–3278, 2002.

Chabbert C, Chambard JM, Sans A, Desmadryl G. Three types of depolarization-activated potassium currents in acutely isolated mouse vestibular neurons. *J Neurophysiol* 85: 1017–1026, 2001.

Chen JWY, Eatock RA. Major potassium conductance in type I hair cells from rat semicircular canals: characterization and modulation by nitric oxide. *J Neurophysiol* 84: 139–151, 2000.

Contini D, Holstein GR, Art JJ. Synaptic cleft microenvironment influences potassium permeation and synaptic transmission in hair cells surrounded by calyx afferents in the turtle. *J Physiol* 598: 853–889, 2020.

Corey DP, Akyuz N, Holt JR. Function and dysfunction of TMC channels in inner ear hair cells. *Cold Spring Harb Perspect Med* 9: a033506, 2019.

Corns LF, Johnson SL, Kros CJ, Marcotti W. Calcium entry into stereocilia drives adaptation of the mechano-electrical transducer current of mammalian cochlear hair cells. *Proc Natl Acad Sci USA* 111: 14918–14923, 2014.

Correia MJ, Lang DG. An electrophysiological comparison of solitary type I and type II vestibular hair cells. *Neurosci Lett* 116: 106–111, 1990.

Crambert G, Hasler U, Beggah AT, Yu C, Modyanov NN, Horisberger J-D, Lelièvre L, Geering K. Transport and pharmacological properties of nine different human Na,K-ATPase isozymes. *J Biol Chem* 275: 1976–1986, 2000.

Curtis HJ, Cole KS. Transverse electric impedance of the squid giant axon. *J Gen Physiol* 21: 757–765, 1938.

Desai SS, Zeh C, Lysakowski A. Comparative morphology of rodent vestibular periphery. I. Sacculus and utricular maculae. *J Neurophysiol* 93: 251–266, 2005.

Freeman SA, Desmazières A, Fricker D, Lubetzki C, Sol-Foulon N. Mechanisms of sodium channel clustering and its influence on axonal impulse conduction. *Cell Mol Life Sci* 73: 723–735, 2016.

Geddes LA, Baker LE. The specific resistance of biological material--a compendium of data for the biomedical engineer and physiologist. *Med Biol Eng* 5: 271–293, 1967.

- Gentet LJ, Stuart GJ, Clements JD.** Direct measurement of specific membrane capacitance in neurons. *Biophys J* 79: 314–320, 2000.
- Hodgkin AL, Huxley AF.** A quantitative description of membrane current and its application to conduction and excitation in nerve. *J Physiol* 117: 500–544, 1952.
- Hoffman LF, Honrubia V.** Fiber diameter distributions in the chinchilla's ampullary nerves. *Hear Res* 172: 37–52, 2002.
- Holt JR, Corey DP, Eatock RA.** Mechanoelectrical transduction and adaptation in hair cells of the mouse utricle, a low-frequency vestibular organ. *J Neurosci* 17: 8739–8748, 1997.
- Horwitz GC, Risner-Janiczek JR, Holt JR.** Mechanotransduction and hyperpolarization-activated currents contribute to spontaneous activity in mouse vestibular ganglion neurons. *J Gen Physiol* 143: 481–497, 2014.
- Horwitz GC, Risner-Janiczek JR, Jones SM, Holt JR.** HCN channels expressed in the inner ear are necessary for normal balance function. *J Neurosci* 31: 16814–16825, 2011.
- Hurley KM, Gaboyard S, Zhong M, Price SD, Wooltorton JRA, Lysakowski A, Eatock RA.** M-like K⁺ currents in type I hair cells and calyx afferent endings of the developing rat utricle. *J Neurosci* 26: 10253–10269, 2006.
- Jaisser F, Jaunin P, Geering K, Rossier BC, Horisberger JD.** Modulation of the Na,K-pump function by beta subunit isoforms. *J Gen Physiol* 103: 605–623, 1994.
- Kalluri R, Xue J, Eatock RA.** Ion channels set spike timing regularity of mammalian vestibular afferent neurons. *J Neurophysiol* 104: 2034–2051, 2010.
- Kay AR, Sugimori M, Llinás R.** Kinetic and stochastic properties of a persistent sodium current in mature guinea pig cerebellar Purkinje cells. *J Neurophysiol* 80: 1167–1179, 1998.
- Köppl C, Wilms V, Russell IJ, Nothwang HG.** Evolution of endolymph secretion and endolymphatic potential generation in the vertebrate inner ear. *Brain Behav Evol* 92: 1–31, 2018.
- Korogod N, Petersen CC, Knott GW.** Ultrastructural analysis of adult mouse neocortex comparing aldehyde perfusion with cryo fixation. *eLife* 4: e05793, 2015.
- Lee C-H, MacKinnon R.** Structures of the human HCN1 hyperpolarization-activated channel. *Cell* 168: 111-120.e11, 2017.
- Li Y, Liu H, Zhao X, He DZ.** Endolymphatic potential measured from developing and adult mouse inner ear. *Front Cell Neurosci* 14: 584928–584928, 2020.
- Lide DR, Baysinger G, Berger LI, Goldberg RN, Kehiaian HV, Kuchitsu K, Rosenblatt G, Roth DL, Zwillinger D,** editors. Ionic conductivity and diffusion at infinite dilution. In: *CRC Handbook of Chemistry and Physics*. Boca Raton, FL: CRC Press, 2005.

Lim R, Kindig AE, Donne SW, Callister RJ, Brichta AM. Potassium accumulation between type I hair cells and calyx terminals in mouse crista. *Exp Brain Res* 210: 607–621, 2011.

Liu X-P, Wooltorton JRA, Gaboyard-Niay S, Yang F-C, Lysakowski A, Eatock RA. Sodium channel diversity in the vestibular ganglion: Na_v 1.5, Na_v 1.8, and tetrodotoxin-sensitive currents. *J Neurophysiol* 115: 2536–2555, 2016.

Lysakowski A, Gaboyard-Niay S, Calin-Jageman I, Chatlani S, Price SD, Eatock RA. Molecular microdomains in a sensory terminal, the vestibular calyx ending. *J Neurosci* 31: 10101–10114, 2011.

Marcoux AA, Garneau AP, Frenette-Cotton R, Slimani S, Mac-Way F, Isenring P. Molecular features and physiological roles of K⁺ - Cl⁻ cotransporter 4 (KCC4). *Biochim Biophys Acta (BBA)* 1861: 3154–3166, 2017.

Mercado A, Song L, Vázquez N, Mount DB, Gamba G. Functional comparison of the K⁺-Cl⁻ cotransporters KCC1 and KCC4. *J Biol Chem* 275: 30326–30334, 2000.

Meredith FL, Benke TA, Rennie KJ. Hyperpolarization-activated current (I_h) in vestibular calyx terminals: characterization and role in shaping postsynaptic events. *J Assoc Res Otolaryngol* 13: 745–758, 2012.

Meredith FL, Rennie KJ. Zonal variations in K⁺ currents in vestibular crista calyx terminals. *J Neurophysiol* 113: 264–276, 2015.

Meredith FL, Rennie KJ. Regional and developmental differences in Na⁺ currents in vestibular primary afferent neurons. *Front Cell Neurosci* 12: 423, 2018.

Nicholson C, Phillips JM. Ion diffusion modified by tortuosity and volume fraction in the extracellular microenvironment of the rat cerebellum. *J Physiol* 321: 225–257, 1981.

Quraishi IH. Computational modeling of potassium transport in the inner ear. Rice University 2008.

Rennie KJ, Correia MJ. Potassium currents in mammalian and avian isolated type I semicircular canal hair cells. *J Neurophysiol* 71: 317–329, 1994.

Rennie KJ, Ricci AJ, Correia MJ. Electrical filtering in gerbil isolated type I semicircular canal hair cells. *J Neurophysiol* 75: 2117–2123, 1996.

Ritchie JM, Rogart RB. Density of sodium channels in mammalian myelinated nerve fibers and nature of the axonal membrane under the myelin sheath. *Proc Natl Acad Sci USA* 74: 211–215, 1977.

Roberts WM, Jacobs RA, Hudspeth AJ. The hair cell as a presynaptic terminal. *Ann N Y Acad Sci* 635: 221–233, 1991.

Rüsch A, Eatock RA. A delayed rectifier conductance in type I hair cells of the mouse utricle. *J Neurophysiol* 76: 995–1004, 1996.

Sadeghi SG, Pyott SJ, Yu Z, Glowatzki E. Glutamatergic signaling at the vestibular hair cell calyx synapse. *J Neurosci* 34: 14536–14550, 2014.

Schuth O, McLean WJ, Eatock RA, Pyott SJ. Distribution of Na,K-ATPase α subunits in rat vestibular sensory epithelia. *J Assoc Res Otolaryngol* 15: 739–754, 2014.

Songer JE, Eatock RA. Tuning and timing in mammalian type I hair cells and calyceal synapses. *J Neurosci* 33: 3706–3724, 2013.

Spaiardi P, Tavazzani E, Manca M, Milesi V, Russo G, Prigioni I, Marcotti W, Magistretti J, Masetto S. An allosteric gating model recapitulates the biophysical properties of $I_{K,L}$ expressed in mouse vestibular type I hair cells: Allosteric gating of $I_{K,L}$. *J Physiol* 595: 6735–6750, 2017.

Spaiardi P, Tavazzani E, Manca M, Russo G, Prigioni I, Biella G, Giunta R, Johnson SL, Marcotti W, Masetto S. K^+ accumulation and clearance in the calyx synaptic cleft of type I mouse vestibular hair cells. *Neuroscience* 426: 69–86, 2020.

Spoendlin. Some morphofunctional and pathological aspects of the vestibular sensory epithelia. In: *Second symposium on the role of the vestibular organs in space exploration*. Ames Research Center, Moffet Field, California: NASA, 1966, p. 99–116.

Stämpfli R. Saltatory conduction in nerve. *Physiol Rev* 34: 101–112, 1954.

Ventura CM, Kalluri R. Enhanced activation of HCN channels reduces excitability and spike-timing regularity in maturing vestibular afferent neurons. *J Neurosci* 1811–18, 2019.

Wang K, Zhao Y, Chen D, Fan B, Lu Y, Chen L, Long R, Wang J, Chen J. Specific membrane capacitance, cytoplasm conductivity and instantaneous Young's modulus of single tumour cells. *Scientific Data* 4: 170015, 2017.

Wong WH, Hurley KM, Eatock RA. Differences between the negatively activating potassium conductances of mammalian cochlear and vestibular hair cells. *J Assoc Res Otolaryngol* 5: 270–284, 2004.

Zhou T, Ming Y, Perry SF, Tatic-Lucic S. Estimation of the physical properties of neurons and glial cells using dielectrophoresis crossover frequency. *J Biol Phys* 42: 571–586, 2016.